ACS APPLIED BIO MATERIALS

www.acsabm.org

Article

Biocompatible Co−P Metallic Glasses with Superior Degradation Tolerance in Physiological Environments

Mayur Pole, Kun Man, Chaitanya Mahajan, Shristy Jha, Yong Yang, and Sundeep Mukherjee*

Cite This: *ACS Appl. Bio Mater.* 2024, 7, 238−245

Read Online

ACCESS | Metrics & More | Article Recommendations

ABSTRACT: Metallic glasses represent a class of metallic alloys with a fully amorphous structure and attractive properties, making them promising in bioimplant applications. Here, the degradation tolerance of biocompatible cobalt−phosphorus (Co−P) metallic glasses was studied in a simulated physiological environment. The metallic glasses were synthesized in the form of coatings through a facile electrodeposition approach. This method utilizes their outstanding surface characteristics and bypasses the size limitations usually associated with their bulk counterparts. The Co−P alloys showed exceptional tribological response with ∼14% lower coefficient of friction and 2 orders of magnitude lesser wear rate compared to SS316 stainless steel. In addition, the Co−P alloys showed a 3 times higher hardness and 4 times higher hardness/modulus ratio compared to SS316, indicating better elastic recovery under dynamic shear stresses that are common in load-bearing bioimplants. The Co−P metallic glasses exhibited excellent hemocompatibility and cytocompatibility in terms of lower platelet adhesion, spreading, and aggregation, a hemolysis ratio lower than 1%, and enhanced surface wettability, suggesting a superlative performance in bioimplant applications.

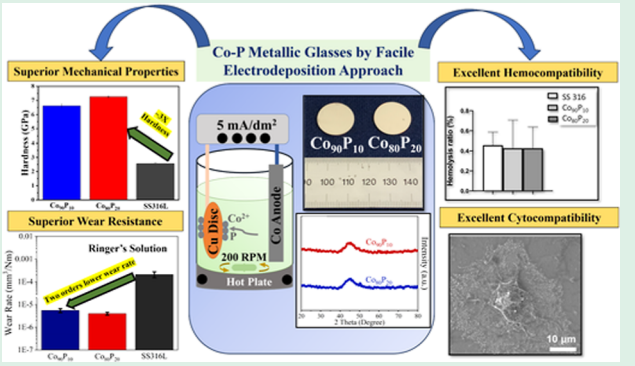

KEYWORDS: *metallic glass, biocompatible, electrodeposition, friction, wear, hemocompatible*

1. INTRODUCTION

The term "bioimplant" is broadly used to describe prostheses used for the repair, replacement, and augmentation of diseased or damaged tissue within the body. Biocompatibility and the ability to function reliably for extended periods of time in a biological milieu are key requirements for such materials. The majority of bioimplants used today are made from ceramics, metals, and polymers. Each of these materials has its own set of functionalities, advantages, and drawbacks. Metals and alloys are especially well suited for orthopedic implants that bear weight, due to their high strength and resistance to fracturing.[1−3] Titanium alloys, stainless steels, and cobalt−chromium (Co−Cr) alloys are the most commonly utilized metals for hip and knee joint replacements, bone plates, and dental implants.[4−7] However, complex fabrication methods and corrosion/wear under physiological conditions limit the long-term use of these metallic implants.[8−11] Stainless steels and Co−Cr alloys are susceptible to abrasion and potential toxicity from Cr, which may necessitate implant replacement or removal surgeries.[12] Steels and titanium alloys are susceptible to localized corrosion in the harsh physiological environment, leading to stress shielding and diminished bone density. The surface deterioration of these alloys results in the buildup of metallic debris in the body's soft tissues, triggering adverse reactions and diminishing their efficacy in tissue repair.[13,14]

Numerous approaches are underway to explore new designs and material combinations for obtaining superior orthopedic implants. Metallic glasses (MGs) constitute a comparatively recent category of metallic materials, showing significant promise for use in bioimplant applications.[15−19] Some of the distinctive characteristics of MGs include high hardness (2−14 GPa) and strength (1.5−3 GPa), outstanding resistance to corrosion and wear, as well as a high elastic limit of up to 2%.[20−22] However, rapid cooling requirements to bypass crystallization impose limitations on size and composition, thereby restricting the widespread use of MGs.[23] These constraints may be circumvented by employing metallic glasses as coatings, allowing the utilization of their exceptional surface properties while avoiding the inherent restrictions associated with their use in bulk form.

Received: September 20, 2023
Revised: December 8, 2023
Accepted: December 12, 2023
Published: December 28, 2023

Electrodeposition is a facile process for obtaining MG coatings that is attractive because of its simplicity, rapid deposition rate, cost-effectiveness, low-temperature operation, and tuning of composition with enhanced surface properties.[24−26] Here, biocompatible Co−P metallic glass coatings were synthesized by a facile electrodeposition approach, and their tribological behavior was evaluated in a simulated physiological environment. There are several studies on the microstructure and wear behavior of Co−P alloys with varying phosphorus content.[27−33] However, there are no reports related to their biocompatibility and performance in a physiological environment. Here, we systematically investigated the tribological response, mechanical properties, and biocompatibility of $Co_{100-x}P_x$ (x = 10 and 20 at. %) amorphous alloys (compositions near the eutectic in the Co−P phase diagram[34]) and compared their performance with stainless steel SS316 under identical conditions. The Co−P amorphous alloys showed excellent mechanical properties and wear resistance under simulated physiological conditions and exhibited remarkable hemocompatibility and cytocompatibility.

2. MATERIALS AND METHODS

2.1. Alloy Synthesis. The Co−P amorphous alloys were synthesized by using a pulse reverse current electrodeposition method with a Dynatronix-MicroStar pulse power supply. Table 1 summarizes the bath composition, made from analytical grade chemicals, and stirred magnetically at 200 rpm for 24 h prior to deposition. A pure cobalt (99.99%) plate, positioned horizontally 2 cm from the substrate, served as the soluble anode. Copper plates, mechanically polished to a 1 μm surface finish, were employed as cathode substrates. An area of 2.83 cm^2 of these plates was exposed to the bath, while the remaining surface was shielded with nonconductive acrylic polish. These substrates were then ultrasonically cleaned in acetone for 10 min, rinsed with distilled water, and chemically activated in 10 wt % HCl for 30 s before immediately starting the electrodeposition. The cathodic current density was adjusted to produce specific alloy compositions with the phosphorus content varying between 10 and 20 at. %. A decrease in the phosphorus content with a higher effective current density suggested an indirect deposition mechanism for phosphorus. Electrodeposition of pure Co was achieved by omitting phosphorus and applying a cathodic current density of 15 A/dm^2 with pulsating current. The deposition duration, ranging from 1 to 16 h based on the desired composition, was calibrated to achieve a coating thickness of approximately 40 μm.

Table 1. Electrodeposition Conditions for Preparing Amorphous Co−P Alloys

Composition of Co−P bath	Quantity (g/L)	Function
Cobalt chloride ($CoCl_2$)	25	Cobalt source
Sodium hypophosphite (NaH_2PO_2)	20	Phosphorus source
Ammonium chloride (NH_4Cl)	20	Conductive salt and pH buffer agent
Sodium dodecyl sulfate ($NaC_{12}H_{25}SO_4$)	0.2	Surfactant
Saccharine ($C_7H_5NO_3S$)	0.3	Surfactant
pH	1.8 ± 0.1	
Temperature	50 ± 2 °C	
Agitation speed	250 rpm	

2.2. Structural Characterization and Thermal Analysis. The structural analysis of the alloys was performed using X-ray diffraction (XRD) on a Rigaku Ultima X-ray diffractometer employing 1.54 Å Cu Kα radiation. Cross-sectional examination of the samples for assessing thickness and elemental distribution was carried out through scanning electron microscopy (SEM, FEI Quanta-ESEM 200), supplemented with energy-dispersive spectroscopy (EDS). The thermal behavior of the samples was evaluated using differential scanning calorimetry (DSC, SDT Q600), within a temperature range of 25−1400 °C and at a heating/cooling rate of 20 °C/min. Calibration of heat flow involved two runs: one with an empty pan and another with a sapphire disc. Throughout these analyses, an inert atmosphere was maintained by flowing argon gas at a rate of 20 μL/min to inhibit sample oxidation.

2.3. Mechanical and Tribological Testing. *2.3.1. Hardness and Modulus Measurements.* The mechanical properties, specifically hardness and modulus, of the electrodeposited alloys were measured by utilizing a TI-Premier nanoindenter (Bruker, Minneapolis, MN, USA) equipped with a diamond Berkovich tip. These measurements were conducted at room temperature using a peak load of 1 N. To ensure statistical reliability, a 4 × 4 array of indents, spaced 100 μm apart, was employed, allowing for the calculation of both average values and standard deviations.

2.3.2. Wear Testing. Wear testing, both sliding and reciprocating, was conducted using an RTEC Universal Reciprocating Tribometer (RTEC Instruments, San Jose, CA, USA) in Ringer's solution. The tests utilized AISI 52100 steel balls with a diameter of 6 mm as the counterface material. The wear behavior was examined over a 60 min duration, with a stroke length of 3.5 mm equating to a 76 m sliding distance, to assess the steady-state friction. A 1000 mL batch of Ringer's solution, heated to 37 °C to replicate physiological conditions, was prepared, with 100 mL allocated per experiment to avoid electrolyte contamination. The remaining solution was constantly stirred at a frequency of 25 Hz, maintaining a temperature of 37 °C for the duration of the experiment. Friction data, specifically the coefficient of friction (COF), was logged using MFT17 software. The wear tracks were then scrutinized using white light interferometry at 10× magnification. 3D profiles of these tracks were stitched together and analyzed for wear volume loss (mm^3) using Gwyddion software. A minimum of three tests were conducted under each condition to determine the average values. Additionally, SEM was employed to characterize the wear tracks, enabling an evaluation of the wear mechanisms.

2.4. Contact Angle Measurements. The surface wettability of the alloys was assessed through contact angle measurements conducted using a CAM-PlusR contact angle goniometer (Chem-Instruments Inc., Fairfield, OH) with a fiber optic light source. For each measurement, a 3 μL droplet of Ringer's solution (equivalent to 2 mm in diameter) was carefully deposited onto the alloy surface using a hypodermic syringe. The droplet was allowed a 10 s stabilization period before taking measurements. These procedures were carried out at room temperature, and for each sample, at least 15 contact angle readings were recorded. To reduce errors stemming from arbitrary tangential alignments, the contact angle was determined by using the patented half-angle method (US Patent 5268733).

2.5. Hemocompatibility. *2.5.1. Platelet Adhesion.* The platelet adhesion test was conducted by following the method described previously.[35] The sample surface was covered with 50 μL of platelet-rich plasma (PRP) (Zen-Bio, US) and incubated at 37 °C for 1 h to allow the platelets in PRP to adhere and spread on the surface. After removal of nonadherent platelets by rinsing gently with phosphate-buffered saline (PBS, Thermo Fisher Scientific, US), the adherent platelets were fixed with 4% paraformaldehyde (PFA, Sigma-Aldrich, US) and 2% glutaraldehyde solution (Fisher Chemical, US) at room temperature for 2 h followed by dehydration with gradient ethanol (30, 50, 70, 90, and 100%) and critical point dry with hexamethyldisilane (HMDS, Electron Microscopy Sciences, US) for 10 min, respectively. The samples were sputtered with gold for SEM observation. The number of adhered platelets was counted from at least six SEM images for each sample.

2.5.2. Hemolysis Test. Initially, healthy human blood with 3.8% sodium citrate (Zen-Bio, US) was diluted in a 0.9% sodium chloride solution at a 4:5 volume-to-volume ratio. For each test group, three samples measuring 5 mm × 5 mm × 2 mm were immersed in 9.8 mL

https://doi.org/10.1021/acsabm.3c00844
ACS Appl. Bio Mater. 2024, 7, 238−245

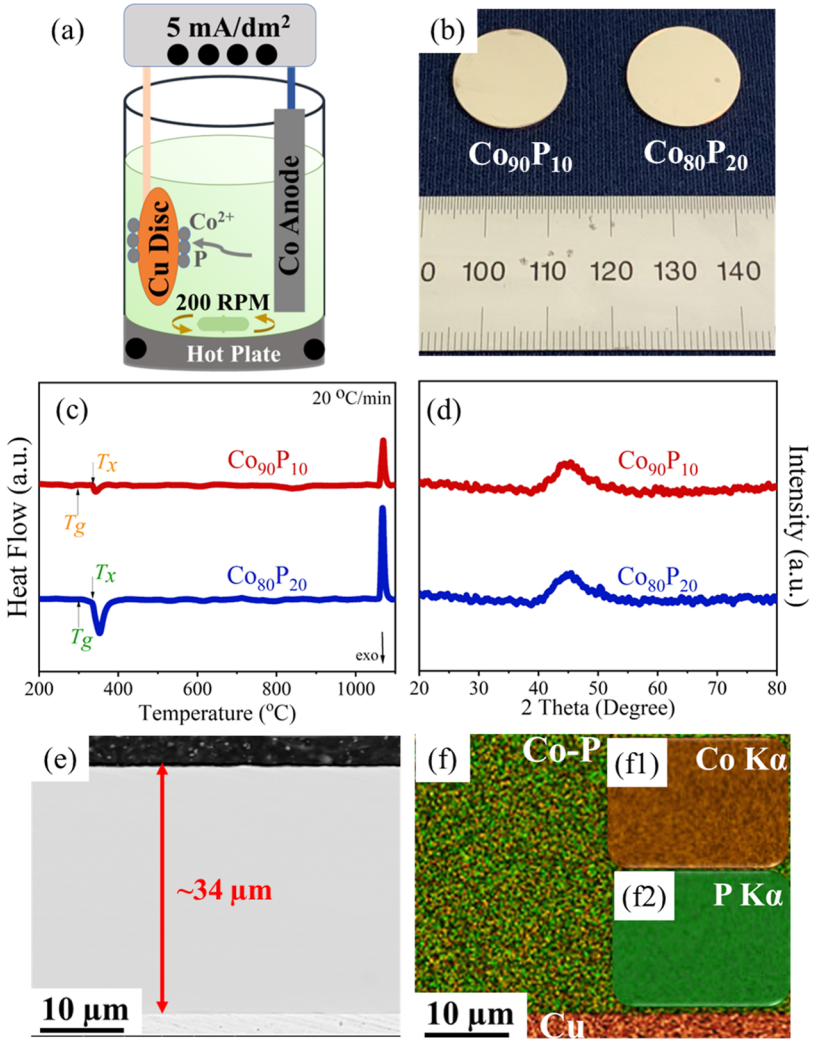

Figure 1. Synthesis and structural characterization: (a) schematic showing electrodeposition of the Co−P amorphous alloy coatings; (b) Optical image of the Co−P amorphous alloy coatings; (c) DSC plot for electrodeposited amorphous $Co_{90}P_{10}$ and $Co_{80}P_{20}$ alloys recorded at 20 °C/min heating rate which shows the glass transition temperature (T_g) and crystallization temperature (T_x); (d) XRD plot for the electrodeposited $Co_{90}P_{10}$, and $Co_{80}P_{20}$ alloys, indicating an amorphous structure because of the broad diffraction peak; (e) SEM image representing the cross-section of electrodeposited $Co_{80}P_{20}$ alloy showing uniform and smooth surface with an average thickness of ~34 μm; and (f) EDS map of the same cross-section indicating a uniform distribution of (f1) Co and (f2) P.

of 0.9% sodium chloride solution within a centrifuge tube and incubated at 37 °C for 30 min. Subsequently, 200 μL of the diluted blood was added to each tube, followed by further incubation at 37 °C for 1 h. As controls, solutions comprising 200 μL of diluted blood in either 9.8 mL of deionized water (positive control) or 0.9% sodium chloride solution (negative control) were prepared. Postincubation, the tubes were centrifuged at 3000 rpm for 5 min, and the supernatants were collected. The absorbance (A) of these solutions was then measured at a wavelength of 545 nm using a Cytation 5 Cell Imaging Multi-Mode Reader (BioTek, US). The hemolysis ratio (HR) was determined using the following formula

$$\mathrm{HR}(\%) = \frac{A_{\mathrm{sample}} - A_{\mathrm{negative}}}{A_{\mathrm{positive}} - A_{\mathrm{negative}}} \times 100\% \quad (1)$$

2.6. Cytocompatibility. The murine calvarial preosteoblasts (MC3T3-E1, ATCC CRL-2593, US) were cultured in minimum essential medium alpha (MEM-α, Gibco, US), enriched with 10% fetal bovine serum (Gibco, US) and a combination of 100 U/mL penicillin and 100 μg/mL streptomycin (Life Technologies, US), in an environment maintained at 37 °C with 5% CO_2. The samples were sterilized using 70% v/v ethanol for an hour, subjected to UV exposure for another hour, and subsequently rinsed with PBS. The cells were then plated onto the samples at a density of 10,000 cells/cm^2 and incubated for 3 days in preparation for cytocompatibility testing.

For cell viability assessment, the samples were first cleansed with PBS. The cells were then detached from the surface using 0.05% trypsin/EDTA (Corning, US), and the enzymatic reaction was stopped using a cell culture medium. The cell suspension was mixed with an equal volume of 0.4% trypan blue (Gibco, US), and both total and blue-stained cells for each sample were counted using a Countess II automated cell counter (Invitrogen, US). Cell viability was determined using a specific eq (eq 2), and this counting process was repeated three times for each sample group

$$\text{Cell viability } (\%) = \left(1 - \frac{\text{number of blue cells}}{\text{number of total cells}}\right) \times 100\% \quad (2)$$

To check the cell morphology, the cells were fixed, dehydrated, and dried by the same method as described in 2.5.1, and the cell morphology was observed using SEM (secondary electron (SE) mode).

2.7. Statistical Analysis. The data are presented as the mean ± standard deviation. Statistical evaluations were conducted using the two-tailed t-test with GraphPad Prism software (GraphPad Software,

https://doi.org/10.1021/acsabm.3c00844
ACS Appl. Bio Mater. 2024, 7, 238−245

Table 2. Mechanical Properties of the CoP Metallic Glasses Compared to SS316[42]

Composition	Hardness (H) (GPa)	Modulus (E) (GPa)	H/E	H^3/E^2 (GPa)	Contact angle (deg)
SS316	2.56 ± 0.07	191 ± 2	0.013	0.00045	60 ± 1.6
$Co_{90}P_{10}$	6.62 ± 0.14	155 ± 2	0.042	0.012	65 ± 1.2
$Co_{80}P_{20}$	7.26 ± 0.05	148 ± 1	0.049	0.017	51 ± 1.2

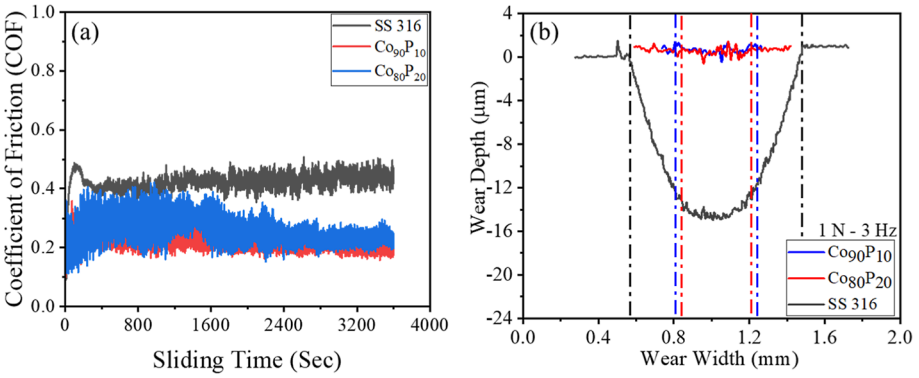

Figure 2. (a) COF vs sliding time for the Co−P electrodeposited alloys and SS316 tested at 1 N load and 3 Hz sliding frequency in Ringer's solution; (b) wear track cross-section profiles at normal loads of 1 N and 3 Hz sliding frequency indicating significantly smaller wear track dimensions for the electrodeposited alloys compared to SS316.

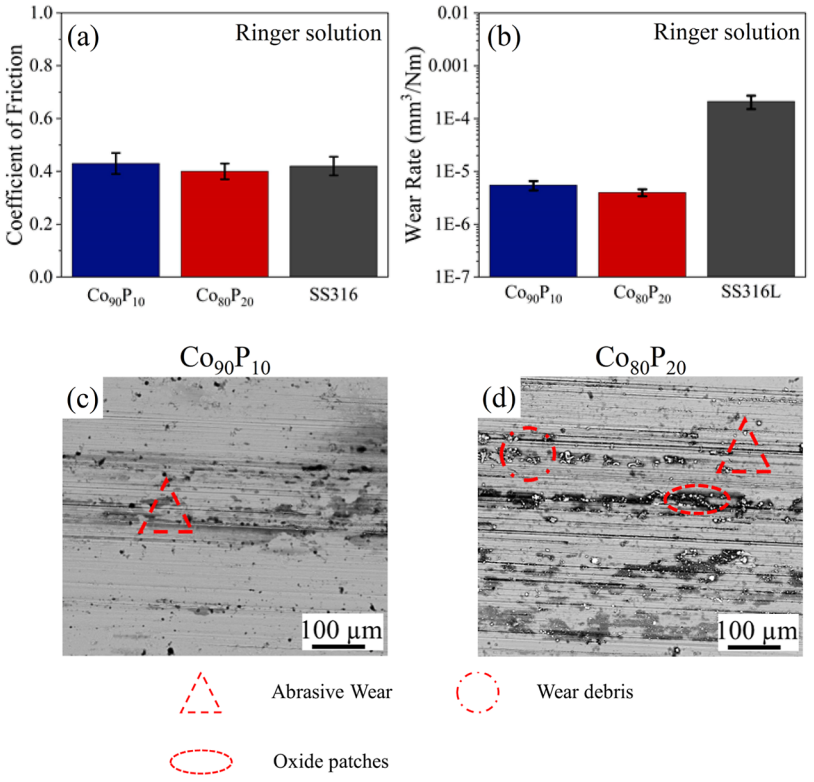

Figure 3. Wear response in a simulated physiological environment: (a) COF and (b) wear rate for the electrodeposited $Co_{100-x}P_x$ metallic glasses and SS316 in Ringer's solution; SEM images of wear tracks at 3 Hz sliding frequency corresponding to 76 m of sliding distance as a function of normal load for (c) $Co_{90}P_{10}$ and (d) $Co_{80}P_{20}$.

US). A p value of less than 0.05 was considered to indicate statistical significance.

3. RESULTS AND DISCUSSION

3.1. Structural Characterization. Structural characterization of the Co−P metallic glasses is summarized in Figure 1. The synthesis of $Co_{90}P_{10}$ and $Co_{80}P_{20}$ amorphous coatings was performed through an electrodeposition approach, and Figure 1a shows the schematic of the setup used. Figure 1b shows the optical image of the electrodeposited $Co_{90}P_{10}$ and $Co_{80}P_{20}$ amorphous coatings, indicating bright and even surfaces. DSC analysis (Figure 1c) shows that the glass transition temperature (T_g) for the two alloys was ~300 °C, crystallization temperature (T_x) was ~330 °C, and the solidus temperature was ~1030 °C in agreement with the Co−P phase diagram.[36] Figure 1d shows the XRD results with broad diffuse diffraction

https://doi.org/10.1021/acsabm.3c00844
ACS Appl. Bio Mater. 2024, 7, 238−245

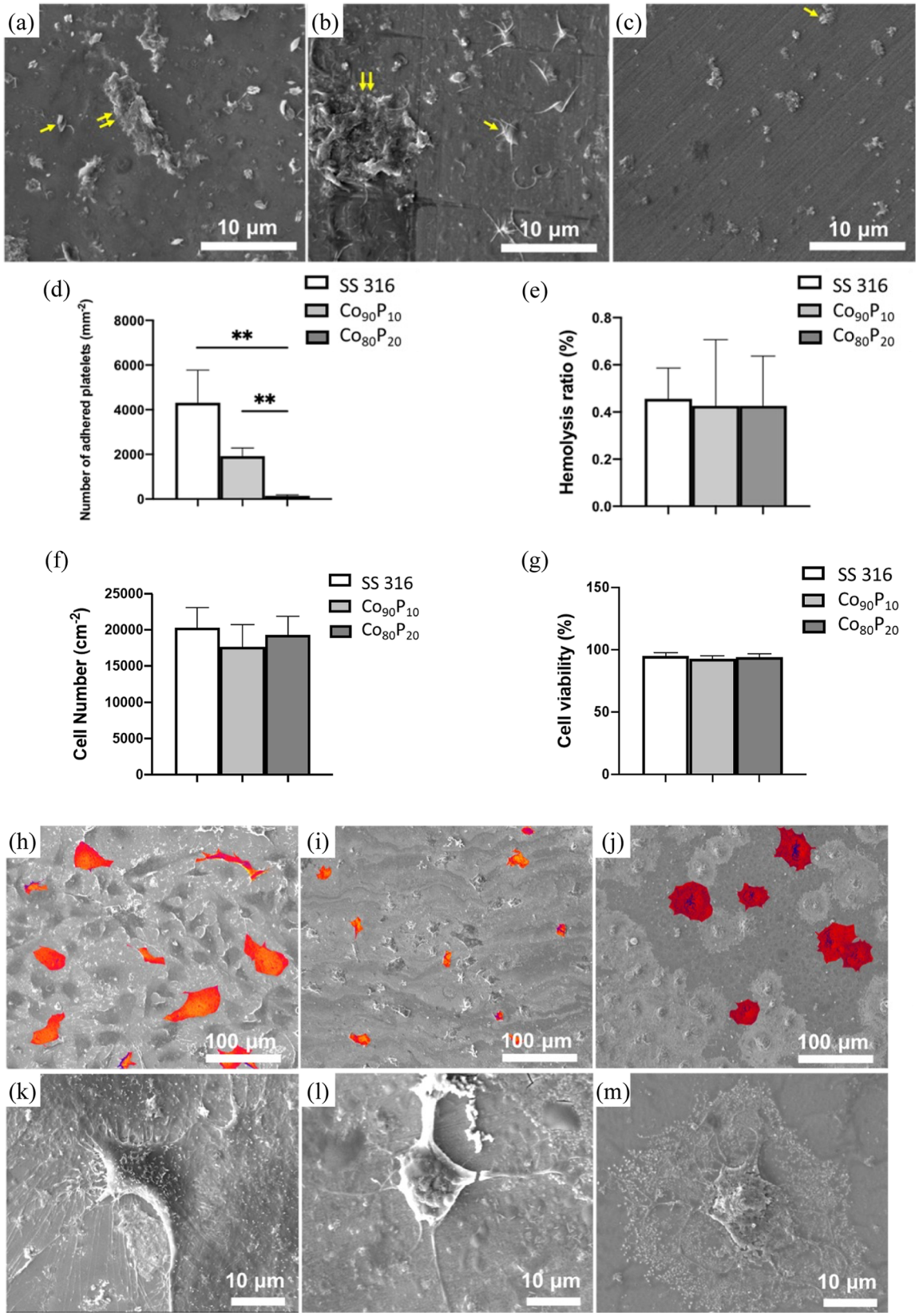

Figure 4. Hemocompatibility and cytocompatibility: hemocompatibility of different samples: (a–c) SEM micrographs of platelets on (a) SS316, (b) $Co_{90}P_{10}$, and (c) $Co_{80}P_{20}$; (d) Number of adhered platelets (n = 6); and (e) Hemolysis ratio on different samples. The single yellow arrowheads point at the platelets, and the double arrowheads point at the platelet aggregates. The significance level is defined as *, $p < 0.05$; **, $p < 0.01$, compared between groups. (f) Cell population and (g) cell viability of preosteoblasts cultured on different samples for 3 days. SEM micrographs of preosteoblasts grown on (h,k) SS316, (i,l) $Co_{90}P_{10}$, and (j,m) $Co_{80}P_{20}$ for 3 days. Some representative cells were falsely colored (red) to display their morphology on these substrates.

https://doi.org/10.1021/acsabm.3c00844
ACS Appl. Bio Mater. 2024, 7, 238–245

peaks, indicating the amorphous nature of the electrodeposited alloys. The shift in the XRD peak to higher 2θ values for the alloy with the higher phosphorus content is attributed to decreased d-spacing in agreement with previous reports.[37] Figure 1e shows a typical cross-sectional SEM image of the $Co_{80}P_{20}$ electrodeposited alloy on a copper substrate, exhibiting a uniform and defect-free deposition, notably devoid of pores. Comparable characteristics, including a consistent average thickness of approximately 35−50 μm, were observed in all of the other electrodeposited alloys. The elemental composition of these alloys, ascertained through EDS, is depicted in Figure 1f. This figure reveals a uniform distribution of the constituent elements, that is, cobalt (shown in Figure 1f1) and phosphorus (illustrated in Figure 1f2).

3.2. Mechanical Behavior. Hardness (H) and modulus (E) for the electrodeposited amorphous $Co_{90}P_{10}$ and $Co_{80}P_{20}$ alloys obtained by nanoindentation at a peak load of 1 N are summarized in Table 2 and compared with SS316 stainless steel. The CoP alloys showed around three times higher hardness compared to SS316, with a higher value for $Co_{80}P_{20}$ (~10% higher) relative to $Co_{90}P_{10}$. The lower modulus for the electrodeposited metallic glasses compared to SS316 may be attributed to reduced atomic packing density and lower atomic bond strength in the amorphous structure.[38] Table 2 summarizes the H/E and H^3/E^2 values for all of the electrodeposited alloys. Here, H/E represents the threshold of elastic behavior in surface contact, while H^3/E^2 is indicative of the material's resistance to plastic deformation under loaded contact.[39,40] Materials with higher H/E and H^3/E^2 ratios typically show better elastic recovery and higher wear resistance under dynamic and shear loading.[41] Here, $Co_{80}P_{20}$ showed ~4 times higher H/E ratio and ~40 times higher H^3/E^2 compared to SS316, indicating superior elastic recovery and wear resistance than SS316.

3.3. Wear Response in a Simulated Physiological Environment. The tribological response of the amorphous $Co_{90}P_{10}$ and $Co_{80}P_{20}$ alloys was evaluated in a simulated physiological environment as summarized in Figures 2 and 3. Figure 2a displays the COF curves relative to the sliding distance for both amorphous alloys and SS316. The amorphous alloys exhibited a shorter initial run-in period compared to SS316. For SS316, a gradual increase in friction was noted over the run-in period, correlating with the extended sliding distance. This run-in behavior is possibly influenced by the elimination of the native oxide layer, the variation in the contact stress due to material wear, and the consequent enlargement of the contact area. Figure 2b shows the 2D cross-sectional wear width and depth profiles for the amorphous $Co_{90}P_{10}$ and $Co_{80}P_{20}$ alloys and SS316 tested at 1 N load in Ringer's solution. The wear track dimensions for SS316 were an order of magnitude larger than those of the amorphous $Co_{90}P_{10}$ and $Co_{80}P_{20}$ alloys. The steady-state COF values, shown in Figure 3a, were 0.42 ± 0.04 for $Co_{90}P_{10}$, 0.38 ± 0.03 for $Co_{80}P_{20}$, and 0.44 ± 0.05 for SS316. These COF values are ~40% lower than that of the Co-28Cr-6Mo alloy tested in Ringer's solution.[43] The wear rates for the two electrodeposited alloys at a 1 N load are summarized in Figure 3b and compared with SS316. The $Co_{100-x}P_x$ alloys showed 2 orders of magnitude lower wear rate compared to SS316. The higher material removal for SS316 compared with the Co−P electrodeposited alloys may be attributed to a larger contact area and lower hardness. Among the $Co_{100-x}P_x$ electrodeposited alloys, $Co_{80}P_{20}$ was marginally more wear-resistant compared to $Co_{90}P_{10}$. These wear rates are comparable to the wear rate for the Co-28Cr-6Mo alloy tested at 5 N load in Ringer's solution.[43] SEM images of the wear tracks for the two electrodeposited alloys at 1 N load and 3 Hz sliding frequency are shown in Figure 3c,d. The predominant wear mechanism for $Co_{90}P_{10}$ at 1 N load was abrasive wear with mild discontinuous oxide patches and surface cavities as shown in Figure 3c. The worn surface was relatively smooth with few grooves due to lubrication in Ringer's solution. The small cavities in the wear track for $Co_{90}P_{10}$ support its increased wear rate compared to $Co_{80}P_{20}$. Figure 3d shows that the dominant wear mechanism for $Co_{80}P_{20}$ at a 1 N load was abrasive wear with fine wear debris compacted on the wear track and discontinuous dark oxide patches. Furthermore, a degree of plastic deformation along with the presence of fine wear debris was noted in certain areas of the wear scar. Following the theory proposed by Bowden and Tabor, the friction force (F) is the product of the sliding contact area (A) and the shear strength (τ) of the sliding interface. Consequently, the COF can be expressed using the following relationship

$$\mathrm{COF} = \frac{F}{W} = \frac{A \cdot \tau}{W} = \frac{\tau}{P_H} \tag{3}$$

where W is the normal force (load) and P_H is the mean Hertzian contact pressure (stress).

3.4. Hemocompatibility and Cytocompatibility. Blood compatibility for the $Co_{100-x}P_x$ electrodeposited alloys was investigated via platelet adhesion and hemolysis assays and compared with that of SS316 stainless steel. Figure 4a−c shows the platelets adhered on the sample surfaces. For SS316, many platelets were observed adhered to the surface with long pseudopodia and some platelets formed aggregates. There were fewer platelets adhered on the $Co_{90}P_{10}$ alloy surface, but platelet spreading and aggregation are evident. Conversely, the number of adhered platelets for the $Co_{80}P_{20}$ alloy was significantly lower, and no spreading and aggregation of platelets was observed. The number of platelets for these surfaces showed a decreasing trend, following the order of SS316 > $Co_{90}P_{10}$ > $Co_{80}P_{20}$ (Figure 4d).

Because platelet adhesion, spreading, and aggregation are key parameters of platelet activation and are considered as the major mechanism for thrombosis, the results from this study suggest that the incorporation of phosphorus could potentially alleviate thrombus formation. These observations agree with a previous report demonstrating that materials containing phosphorus improved hemocompatibility and protein adsorption resistance.[44] The presence of phosphorus may weaken the interactions between the substrate and the plasma proteins and reduce substrate effects on the absorbed protein conformation and enhance blood compatibility.[45] The hemolysis ratio for all of the samples was less than 1% (Figure 4e). This indicates that neither SS316 nor the $Co_{100-x}P_x$ alloys were hemolytic according to the American Society for Testing and Materials (ASTM) F 756-08. Together, these results suggest that all $Co_{100-x}P_x$ alloys were blood compatible and the alloy with the higher phosphorus content had better hemocompatibility.

The 3-(4,5-dimethyl-2-thiazolyl)-2,5-diphenyl-2H-tetrazolium bromide and tetrazolium-8-[2-(2-methoxy-4-nitrophenyl)-3-(4-nitrophenyl)-5-(2,4-disulfophenyl)-2H-tetrazolium] monosodium salt (CCK-8) assays have been widely used for the cell viability test,[46] and the color change that resulted from the sample corrosion was found to interfere with the absorbance measurement. Indeed, the trypan blue test is a

https://doi.org/10.1021/acsabm.3c00844
ACS Appl. Bio Mater. 2024, 7, 238−245

traditional and convenient assay for determining cell viability[47] and thus, the cell viability was assessed using the trypan blue exclusion assay. As shown in Figure 4f,g, after culturing preosteoblasts on the alloys for 3 days, there was no notable difference in cell population across the substrates, and cell viability on all of them exceeded 90%. The cells on the $Co_{80}P_{20}$ alloy displayed larger spreading than those on SS316 and $Co_{90}P_{10}$ (Figure 4h−m). These results suggest that the $Co_{80}P_{20}$ alloy enhanced preosteoblast adhesion compared to SS316 and the $Co_{90}P_{10}$ alloy. Furthermore, we evaluated the wettability of these substrates. Although the contact angle for $Co_{90}P_{10}$ (65 ± 1.2°) was higher than that of SS316 (60 ± 1.6°), an increase in the phosphorus content resulted in a lower contact angle of 51 ± 1.2° for $Co_{80}P_{20}$ as shown in Table 2. This indicates that the higher phosphorus content enhanced the surface wettability of Co−P alloys and thus promoted cell spreading as shown in Figure 4. The correlation between surface wettability and cell spreading suggests that the more hydrophilic surface of $Co_{80}P_{20}$ promoted cell attachment and spreading. In summary, both Co−P alloys were found to have good cytocompatibility and the higher phosphorus content was seen to promote better cell adhesion and growth.

4. CONCLUSIONS

The tribological behavior of $Co_{100-x}P_x$ alloys was studied systematically as a function of composition in a simulated physiological environment and was compared to SS316. In addition, hemocompatibility and cytocompatibility were evaluated. The following conclusions may be drawn:

- The amorphous structure was achieved for the $Co_{100-x}P_x$ electrodeposited alloys for phosphorus in the range of 10 to 20 at. %.
- The $Co_{100-x}P_x$ alloys showed almost threefold higher hardness ($Co_{90}P_{10}$ −6.62 GPa; $Co_{80}P_{20}$ −7.26 GPa) compared to that of SS316 (2.56 GPa), which enhanced their surface degradation resistance.
- Low friction coefficients and wear rates were observed for the $Co_{100-x}P_x$ alloys in a simulated physiological environment with abrasive wear and discontinuous oxide patches as the predominant wear mechanisms.
- The $Co_{100-x}P_x$ (x = 10, 20 at. %) electrodeposited alloys showed good blood compatibility. The alloy with the higher phosphorus content had better hemocompatibility and promoted cell adhesion and growth.

AUTHOR INFORMATION

Corresponding Author

Sundeep Mukherjee − *Department of Materials Science and Engineering, University of North Texas, Denton, Texas 76203, United States;* orcid.org/0000-0002-1954-0045; Phone: 940-565-4170; Email: sundeep.mukherjee@unt.edu; Fax: 940-565-2944

Authors

Mayur Pole − *Department of Materials Science and Engineering, University of North Texas, Denton, Texas 76203, United States; Physical and Computational Sciences Directorate, Pacific Northwest National Laboratory, Richland, Washington 99352, United States*

Kun Man − *Department of Biomedical Engineering, University of North Texas, Denton, Texas 76203, United States;* orcid.org/0000-0002-3764-3312

Chaitanya Mahajan − *Department of Materials Science and Engineering, University of North Texas, Denton, Texas 76203, United States;* orcid.org/0000-0002-9490-2181

Shristy Jha − *Department of Materials Science and Engineering, University of North Texas, Denton, Texas 76203, United States*

Yong Yang − *Department of Biomedical Engineering, University of North Texas, Denton, Texas 76203, United States;* orcid.org/0000-0003-4305-8029

Complete contact information is available at: https://pubs.acs.org/10.1021/acsabm.3c00844

Notes

The authors declare no competing financial interest.

ACKNOWLEDGMENTS

This work was partly supported by funding from the National Science Foundation (NSF) under grant nos. 1561886, 1919220, and 1762545. Any opinions, findings, and conclusions expressed in this paper are those of the authors and do not necessarily reflect the views of the National Science Foundation (NSF).

REFERENCES

(1) Niinomi, M. Recent Metallic Materials for Biomedical Applications. *Metall. Mater. Trans. A* **2002**, *33* (3), 477−486.

(2) Geetha, M.; Singh, A. K.; Asokamani, R.; Gogia, A. K. Ti Based Biomaterials, the Ultimate Choice for Orthopaedic Implants-A Review. *Prog. Mater. Sci.* **2009**, *54* (3), 397−425.

(3) Long, M.; Rack, H. J. Titanium Alloys in Total Joint Replacement-a Materials Science Perspective. *Biomaterials* **1998**, *19* (18), 1621−1639.

(4) Shah, F. A.; Trobos, M.; Thomsen, P.; Palmquist, A. Commercially Pure Titanium (Cp-Ti) versus Titanium Alloy (Ti6Al4V) Materials as Bone Anchored Implants-Is One Truly Better than the Other? *Mater. Sci. Eng., C* **2016**, *62*, 960−966.

(5) Chen, Q.; Thouas, G. A. Metallic Implant Biomaterials. *Mater. Sci. Eng. R Rep.* **2015**, *87*, 1−57.

(6) Lohberger, B.; Stuendl, N.; Glaenzer, D.; Rinner, B.; Donohue, N.; Lichtenegger, H. C.; Ploszczanski, L.; Leithner, A. CoCrMo Surface Modifications Affect Biocompatibility, Adhesion, and Inflammation in Human Osteoblasts. *Sci. Rep.* **2020**, *10* (1), 1682.

(7) Li, H. F.; Zheng, Y. F. Recent Advances in Bulk Metallic Glasses for Biomedical Applications. *Acta Biomater.* **2016**, *36*, 1−20.

(8) Pandey, A. K.; Kumar, A.; Kumar, R.; Gautam, R. K.; Behera, C. K. Tribological Performance of SS 316L, Commercially Pure Titanium, and Ti6Al4V in Different Solutions for Biomedical Applications. *Mater. Today Proc.* **2023**, *78*, A1−A8.

(9) Dearnley, P. A.; Dahm, K. L.; Çimenoğlu, H. The Corrosion-Wear Behaviour of Thermally Oxidised CP-Ti and Ti-6Al-4V. *Wear* **2004**, *256* (5), 469−479.

(10) Kaur, M.; Singh, K. Review on Titanium and Titanium Based Alloys as Biomaterials for Orthopaedic Applications. *Mater. Sci. Eng., C* **2019**, *102*, 844−862.

(11) Costa, B. C.; Tokuhara, C. K.; Rocha, L. A.; Oliveira, R. C.; Lisboa-Filho, P. N.; Costa Pessoa, J. Vanadium Ionic Species from Degradation of Ti-6Al-4V Metallic Implants: In Vitro Cytotoxicity and Speciation Evaluation. *Mater. Sci. Eng., C* **2019**, *96*, 730−739.

(12) Narushima, T.; Ueda, K.; Alfirano Co-Cr Alloys as Effective Metallic Biomaterials. *Advances in metallic biomaterials: tissues, materials and biological reactions*; Springer, 2015; Vol. 3, pp 157−178.

(13) Schmalzried, T. P.; Jasty, M.; Harris, W. H. Periprosthetic Bone Loss in Total Hip Arthroplasty. Polyethylene Wear Debris and the Concept of the Effective Joint Space. *J. Bone Joint Surg.* **1992**, *74* (6), 849−863.

(14) Ibrahim, M. Z.; Sarhan, A. A. D.; Yusuf, F.; Hamdi, M. Biomedical Materials and Techniques to Improve the Tribological, Mechanical and Biomedical Properties of Orthopedic Implants-A Review Article. *J. Alloys Compd.* **2017**, *714*, 636−667.
(15) Inoue, A. Stabilization of Metallic Supercooled Liquid and Bulk Amorphous Alloys. *Acta Mater.* **2000**, *48* (1), 279−306.
(16) Ashby, M. F.; Greer, A. L. Metallic Glasses as Structural Materials. *Scr. Mater.* **2006**, *54* (3), 321−326.
(17) Kim, Y. C.; Bae, D. H.; Kim, W. T.; Kim, D. H. Glass Forming Ability and Crystallization Behavior of Ti-Based Amorphous Alloys with High Specific Strength. *J. Non-Cryst. Solids* **2003**, *325* (1−3), 242−250.
(18) Morrison, M. L.; Buchanan, R. A.; Peker, A.; Liaw, P. K.; Horton, J. A. Electrochemical Behavior of a Ti-Based Bulk Metallic Glass. *J. Non-Cryst. Solids* **2007**, *353* (22−23), 2115−2124.
(19) Zhou, Z.; Wei, Q.; Li, Q.; Jiang, B.; Chen, Y.; Sun, Y. Development of Co-Based Bulk Metallic Glasses as Potential Biomaterials. *Mater. Sci. Eng., C* **2016**, *69*, 46−51.
(20) Greer, A. L.; Rutherford, K. L.; Hutchings, I. M. Wear Resistance of Amorphous Alloys and Related Materials. *Int. Mater. Rev.* **2002**, *47* (2), 87−112.
(21) Schuh, C. A.; Hufnagel, T. C.; Ramamurty, U. Mechanical Behavior of Amorphous Alloys. *Acta Mater.* **2007**, *55* (12), 4067−4109.
(22) Sadeghilaridjani, M.; Ayyagari, A.; Muskeri, S.; Hasannaeimi, V.; Jiang, J.; Mukherjee, S. Small-Scale Mechanical Behavior of Ion-Irradiated Bulk Metallic Glass. *Jom* **2020**, *72*, 123−129.
(23) Hofmann, D. C.; Suh, J. Y.; Wiest, A.; Duan, G.; Lind, M. L.; Demetriou, M. D.; Johnson, W. L. Designing Metallic Glass Matrix Composites with High Toughness and Tensile Ductility. *Nature* **2008**, *451* (7182), 1085−1089.
(24) Bekish, Y. N.; Poznyak, S. K.; Tsybulskaya, L. S.; Gaevskaya, T. V. Electrodeposited Ni-B Alloy Coatings: Structure, Corrosion Resistance and Mechanical Properties. *Electrochim. Acta* **2010**, *55* (7), 2223−2231.
(25) Pole, M.; Sadeghilaridjani, M.; Shittu, J.; Mahajan, C.; Ghodki, N.; Mukherjee, S. Electrodeposited Metallic Glasses with Superlative Wear Resistance. *Mater. Sci. Eng., A* **2021**, *816*, 141315.
(26) Ji, X.; Zhao, J.; Yang, S.; Gu, L. Erosion-Corrosion Behavior of Electrodeposited Amorphous Ni-W-P Coating in Saline-Sand Slurry. *Corrosion* **2013**, *69* (6), 593−600.
(27) Barzegar, M.; Allahkaram, S. R.; Naderi, R.; Ghavidel, N. Effect of Phosphorous Content and Heat Treatment on the Structure, Hardness and Wear Behavior of Co-P Coatings. *Wear* **2019**, *422*−*423*, 35−43.
(28) Sheikholeslam, M. A.; Enayati, M. H.; Raeissi, K. Characterization of Nanocrystalline and Amorphous Cobalt-Phosphorous Electrodeposits. *Mater. Lett.* **2008**, *62* (21−22), 3629−3631.
(29) Erb, U. Electrodeposited Nanocrystalline Cobalt-Phosphorus Alloys-An Advanced Alternative to Hard Chrome Plating for Non-Line of Sight Coating Applications *AESF/EPA Conference for Environmental & Process Excellence*, 2003.
(30) Weston, D. P.; Shipway, P. H.; Harris, S. J.; Cheng, M. K. Friction and Sliding Wear Behaviour of Electrodeposited Cobalt and Cobalt-Tungsten Alloy Coatings for Replacement of Electrodeposited Chromium. *Wear* **2009**, *267* (5−8), 934−943.
(31) Li, R.; Hou, Y.; Dong, Q.; Su, P.; Ju, P.; Liang, J. Wear and Corrosion Resistance of Co-P Coatings: The Effects of Current Modes. *RSC Adv.* **2018**, *8* (2), 895−903.
(32) Safavi, M. S.; Walsh, F. C. Electrodeposited Co-P Alloy and Composite Coatings: A Review of Progress towards Replacement of Conventional Hard Chromium Deposits. *Surf. Coat. Technol.* **2021**, *422*, 127564.
(33) Prado, R. A.; Benfer, J.; Mahalanobis, N.; Legg, K.; Jacksonville, N. A. S. C. F. *Electrodeposited Nanocrystalline Co-P Alloy Coatings as a Hard Chrome Alternative. ESTCP Project WP-200936*, 2015, p 1.
(34) Ishida, K.; Nishizawa, T. The Co-P (Cobalt-Phosphorus) System. *Bull. Alloy Phase Diagrams* **1990**, *11* (6), 555−560.
(35) Ho, Y.-H.; Man, K.; Joshi, S. S.; Pantawane, M. V.; Wu, T.-C.; Yang, Y.; Dahotre, N. B. In-Vitro Biomineralization and Biocompatibility of Friction Stir Additively Manufactured AZ31B Magnesium Alloy-Hydroxyapatite Composites. *Bioact. Mater.* **2020**, *5* (4), 891−901.
(36) Ishida, K.; Nishizawa, T. The Co-P (Cobalt-Phosphorus) System. *Bull. Alloy Phase Diagrams* **1990**, *11* (6), 555−560.
(37) Bera, P.; Seenivasan, H.; Rajam, K. S.; William Grips, V. K. Characterization of Amorphous Co-P Alloy Coatings Electrodeposited with Pulse Current Using Gluconate Bath. *Appl. Surf. Sci.* **2012**, *258* (24), 9544−9553.
(38) Wang, J. G.; Choi, B. W.; Nieh, T. G.; Liu, C. T. Crystallization and Nanoindentation Behavior of a Bulk Zr-Al-Ti-Cu-Ni Amorphous Alloy. *J. Mater. Res.* **2000**, *15* (3), 798−807.
(39) Cheng, J.; Liu, D.; Liang, X.; Chen, Y. Evolution of Microstructure and Mechanical Properties of in Situ Synthesized TiC-TiB2/CoCrCuFeNi High Entropy Alloy Coatings. *Surf. Coat. Technol.* **2015**, *281*, 109−116.
(40) Costa, H. L.; Oliveira Junior, M. M.; de Mello, J. D. B. Effect of Debris Size on the Reciprocating Sliding Wear of Aluminium. *Wear* **2017**, *376*−*377*, 1399−1410.
(41) Mo, J. L.; Zhu, M. H.; Leyland, A.; Matthews, A. Impact Wear and Abrasion Resistance of CrN, AlCrN and AlTiN PVD Coatings. *Surf. Coat. Technol.* **2013**, *215*, 170−177.
(42) Singh, R.; Agrahari, S.; Yadav, S. D.; Kumar, A. Microstructural Evolution and Mechanical Properties of 316 Austenitic Stainless Steel by CGP. *Mater. Sci. Eng., A* **2021**, *812*, 141105.
(43) Liu, Y.; Pang, S.; Yang, W.; Hua, N.; Liaw, P. K.; Zhang, T. Tribological Behaviors of a Ni-Free Ti-Based Bulk Metallic Glass in Air and a Simulated Physiological Environment. *J. Alloys Compd.* **2018**, *766*, 1030−1036.
(44) Bowden, F. P.; Tabor, D. *The Friction and Lubrication of Solids*; Oxford University Press, 2001; Vol. *1*.
(45) Kwok, S. C. H.; Wang, J.; Chu, P. K. Surface Energy, Wettability, and Blood Compatibility Phosphorus Doped Diamond-like Carbon Films. *Diam. Relat. Mater.* **2005**, *14* (1), 78−85.
(46) Jiao, G.; He, X.; Li, X.; Qiu, J.; Xu, H.; Zhang, N.; Liu, S. Limitations of MTT and CCK-8 Assay for Evaluation of Graphene Cytotoxicity. *RSC Adv.* **2015**, *5* (66), 53240−53244.
(47) Crowley, L. C.; Marfell, B. J.; Christensen, M. E.; Waterhouse, N. J. Measuring Cell Death by Trypan Blue Uptake and Light Microscopy. *Cold Spring Harb. Protoc.* **2016**, *2016* (7), pdb.prot087155−prot087155.

https://doi.org/10.1021/acsabm.3c00844
ACS Appl. Bio Mater. 2024, 7, 238−245